THE JOURNAL OF PHYSICAL CHEMISTRY A

Article

Cite This: J. Phys. Chem. A 2019, 123, 5906−5917

pubs.acs.org/JPCA

Spectroscopy and Two-Photon Dissociation of Jet-Cooled Pyruvic Acid

Published as part of The Journal of Physical Chemistry virtual special issue "F. Javier Aoiz Festschrift".

Subhasish Sutradhar, Bibek R. Samanta, Ravin Fernando, and Hanna Reisler*

Department of Chemistry, University of Southern California, Los Angeles, California 90089-0482, United States

Supporting Information

ABSTRACT: The UV photodissociation of pyruvic acid (PA) is studied in molecular beams using time-of-flight (TOF) mass spectroscopy and time-sliced velocity map imaging (VMI) following excitation to the first absorption band ($S_1 \leftarrow S_0$) at 330−380 nm. CH_3CO, HOCO, CO, CH_3, and H are detected as photodissociation products. The photofragment yield (PFY) spectrum of the H product is recorded at 350−380 nm in He and Ar carrier gases. The spectrum shows sharp vibrational features reflecting the significant rotational cooling achieved in the molecular beam. It matches well the broad features observed in the room temperature absorption spectrum and indicates that the S_1 state lives longer than a picosecond. The origin band of the $S_1 \leftarrow S_0$ transition is identified at 26 710 cm^{-1}, and progressions in the CH_3 and C−C torsional modes are tentatively assigned. Kinetic energy release (KER) and angular distributions of CH_3CO, HOCO, CO, CH_3, and H fragments indicate that additional photon absorption from S_1 to the S_2/S_3 states is facile and is followed by rapid dissociation to the observed fragments. On the basis of the energetics of the different dissociation pathways and analyses of the observed KER distributions, three-body fragmentation processes are proposed as major contributors to the formation of the observed products.

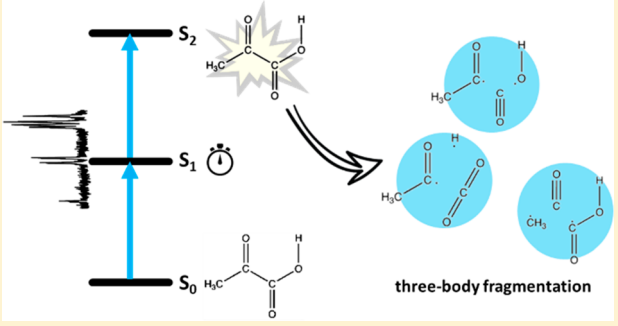

I. INTRODUCTION

Pyruvic acid (PA) is an atmospherically important α-keto carboxylic acid, and as such its UV absorption spectrum and decomposition in the gas phase were studied extensively at wavelengths similar to solar radiation.[1−11] Several investigators reported that the first absorption system of PA in the gas phase lies at 300−380 nm.[1,5,8] This band system accesses the first excited singlet state (S_1) via a $\pi^* \leftarrow n_+$ transition in which an electron in a nonbonding lone pair of the carbonyl oxygen is promoted to an antibonding orbital, resulting in electron density primarily along the central C−C bond.[11] Although a high-resolution 298 K absorption spectrum of PA at 1.2 Torr has been reported by Horowitz et al., the vibronic bands were too broad and overlapped for spectroscopic assignments.[8] Yamamoto and Back observed light emission at the same wavelengths at 1−10 Torr and 340 K and inferred that the S_1 state is relatively long-lived, especially at long excitation wavelengths where the emission was more intense.[1]

Previous photolysis studies of PA performed at low pressures (1−10 Torr) at $\lambda < 366$ nm showed that decarboxylation leading to CO_2 and CH_3CHO final products is the predominant photodissociation pathway.[1,6,7] Although a mechanism for the formation of these products has been proposed, the contributions of S_1, T_1, and highly vibrationally excited levels of S_0 to the photodissociation are still under debate. For example, while early studies ruled out the participation of T_1 and vibrationally "hot" S_0 levels in the formation of CO_2 and CH_3CHO,[1] theoretical calculations indicated that decarboxylation happens on S_0 after an efficient conical intersection between S_1 and S_0 and that dissociation on T_1 can be an additional source of these products.[11]

In addition to these low-pressure studies, the photodissociation of PA via S_1 has been investigated at atmospheric pressures in the presence of O_2, N_2, and air.[2−4,10] These studies not only revealed new photodissociation pathways but also showed that the photodissociation quantum yield depended on the initial concentration of PA and the pressure and nature of the buffer gas. For example, Berges and Warneck suggested that photolysis of PA at 350 nm at atmospheric pressure produced significant amounts of CH_3CO and acetic acid.[10] Vaida and co-workers investigated the photodissociation of PA (2−12 ppm) in air and N_2 using broadband radiation similar to the solar flux and found acetic acid as one of the photoproducts.[2]

Whereas previous studies shed light on the final products of PA photodissociation under atmospherically relevant conditions, most of these experiments have been carried out in static gas cells where nascent products are likely to undergo

Received: May 2, 2019
Revised: June 22, 2019
Published: June 25, 2019

DOI: 10.1021/acs.jpca.9b04166
J. Phys. Chem. A 2019, 123, 5906−5917

secondary reactions due to multiple collisions. Not surprisingly, under these conditions, the final products and their yields found in the different studies depended on the concentration of PA, the pressure in the reaction chamber, and the specific experimental arrangement used in each study. These studies do not always agree with one another on the relative abundances of the final products.[2−4,10] The results indicate that the relaxation of the S_1 state and its coupling to S_0 and/or T_1 may be sensitive to pressure. Clearly, information on the photophysics and photochemistry of PA in the pristine collisionless environment of molecular beams is desirable. Here we report our first study of the $S_1 \leftarrow S_0$ absorption spectrum obtained in molecular beams and the products detected following two-photon dissociation via the S_1 state.

The molecular beam absorption spectrum of PA has not been measured before because the $S_1 \leftarrow S_0$ absorption system is fairly weak,[1,8] and the proposed nascent products, CO_2 and methylhydroxycarbene (CH_3COH), are not easily detected. However, we discovered that due to its relatively long lifetime, a second photon absorption by S_1 is facile, leading to several photoproducts that can be detected by ionization. In this paper we report the molecular beam photofragment yield (PFY) spectrum and multiphoton dissociation of PA at 350−380 nm, using He and Ar carrier gases. CH_3CO, HOCO, CO, CH_3, and H products were detected by time-of-flight (TOF) mass spectroscopy and velocity map imaging (VMI). The PFY spectra of the products mapped the broad absorption peaks of PA observed at room temperature, but the rovibronic bands exhibited significant rotational cooling and were well resolved. The two-photon nature of formation of the fragments was confirmed by their kinetic energy release (KER) distributions measured by monitoring CH_3CO, HOCO, CO, CH_3, and H products. We find that three-body fragmentation is a major dissociation mechanism leading to the observed products.

The paper is organized as follows. In sections II and III we describe the experimental details and results, and list the energetically allowed pathways. We start section IV by presenting electronic structure calculations of the excited states of PA, followed by discussion of the $S_1 \leftarrow S_0$ spectroscopy and the probability of absorption of a second photon by the S_1 state. We then turn our attention to the two-photon dissociation reactions and discuss possible two- and three-body fragmentation pathways. We end the discussion by proposing the most plausible dissociation mechanisms. Section V provides summary and conclusions.

II. EXPERIMENTAL SECTION

Pyruvic acid (PA) (98%, Sigma-Aldrich) is purified by vacuum distillation at 50−60 °C twice, and the distilled colorless sample is then degassed using several freeze−pump−thaw cycles.[3] PA vapor is introduced into the source region of the vacuum chamber by bubbling a carrier gas (He or Ar) through the sample at 1300 Torr and supersonically expanding the mixture through a piezoelectrically driven pulsed nozzle operating at 10 Hz. After passing through a skimmer (Beam Dynamics, 1.0 mm diameter), PA is excited by UV laser radiation (330−380 nm, 2−3 mJ/pulse, focused by a 30 cm focal-length (f.l.) lens to about 0.1 mm) from the frequency doubled output of a dye laser (Continuum ND6000, DCM dye) pumped by the second harmonic output of a pulsed Nd:YAG laser (Continuum, PL8000). The fluence in the 10 ns pulse used in this experiment is about 6×10^{19} photons cm^{-2}. H, CH_3CO, HOCO, CO, and CH_3 photofragments are detected by TOF mass spectroscopy and VMI using the appropriate probe laser radiation.

H photofragments are probed by 1+1′ two-color resonance enhanced multiphoton ionization (REMPI) via the Lyman-α transition. The required vacuum ultraviolet (VUV) laser radiation at 121.567 nm is generated by frequency tripling of ∼365 nm (2−3 mJ) radiation focused into a gas mixture of Kr:Ar = 200:590 Torr in a stainless steel cell. The 365 nm radiation is generated by frequency doubling the output of a dye laser (Continuum, ND6000, LDS 722 dye) pumped with 532 nm laser radiation (second harmonic of a Nd:YAG laser; Continuum, NY-81C). The VUV and residual 365 nm beams are focused into the chamber using a MgF_2 lens (f.l. = 7.5 cm).

Because there are no known REMPI detection schemes for CH_3CO and HOCO, these photofragments are detected by one-color multiphoton nonresonant ionization, in which the pump radiation also ionizes the photofragments. The non-state selective detection can encompass all the internal states of these species that are below their barriers to dissociation (6000 cm^{-1} for CH_3CO and 9000 cm^{-1} for HOCO). CO ($X\ ^1\Sigma^+$, $v'' = 0, 1$) products are detected by 2+1 REMPI at 230.1−230.5 nm via the $B\ ^1\Sigma^+ \leftarrow X\ ^1\Sigma^+$ transition.[12] The UV radiation is generated by the frequency doubled output of a dye laser (Continuum ND6000, Coumarin dyes, 0.5−1 mJ/pulse) pumped by the third harmonic output of a pulsed Nd:YAG laser (Continuum, PL8000).

CH_3 ($\tilde{X}\ ^2A_2''$, $v_1''\ v_2''\ v_3''\ v_4''$) products are detected by 2+1 REMPI at 325−336 nm (∼1 mJ/pulse) via the $3p\ ^2A_2'' \leftarrow \tilde{X}\ ^2A_2''$ transition.[13,14]

Detailed description and performance characteristics of the time-sliced VMI apparatus are given elsewhere.[15−17] Briefly, the ions produced in the detection region are accelerated in the TOF tube through a series of electrostatic lenses toward a position sensitive detector (40 mm dia double-stack microchannel plates) coupled to a phosphor screen (Galileo Electro-Optics 3040FM series). Ion hit events on the detector are recorded by a 1 megapixel digital video-camera (PixeLINK PL-B741F) located behind the phosphor screen, and the data are transferred to a computer for further analysis. Time-sliced images of the ion sphere are obtained by fast gating of the detector (back plate of the MCP) using a home-built high-voltage pulser (5 ns fwhm, 2 kV peak).[15]

III. RESULTS

III.A. Photofragment Yield Spectra. Atomic hydrogen photofragments were produced by two-photon dissociation via the S_1 state (see below). H-photofragment yield (H-PFY) spectra were recorded in He or Ar as a carrier gas by scanning the pump laser radiation from 330 to 380 nm while the probe laser radiation was fixed to detect H photofragments. The recorded spectra show significant rovibrational cooling of PA in the molecular beam. As seen in Figure 1, the vibronic peaks in the H-PFY spectrum recorded in He match well the broad $S_1 \leftarrow S_0$ absorption features recorded at 298 K. The corresponding spectrum recorded in Ar and shown in Figure 2 achieves even greater rotational cooling. Both spectra become progressively congested toward shorter wavelengths.

It is important to note the difference between the absorption and the H-PFY spectra shown in Figures 1 and 2. The spectral intensities and vibrational progressions observed in the 298 K absorption spectrum depend on the rovibrational populations of S_0 and the Franck−Condon factors for the $S_1 \leftarrow S_0$ transition. The cold molecular beam PFY spectrum originates

DOI: 10.1021/acs.jpca.9b04166
J. Phys. Chem. A 2019, 123, 5906−5917

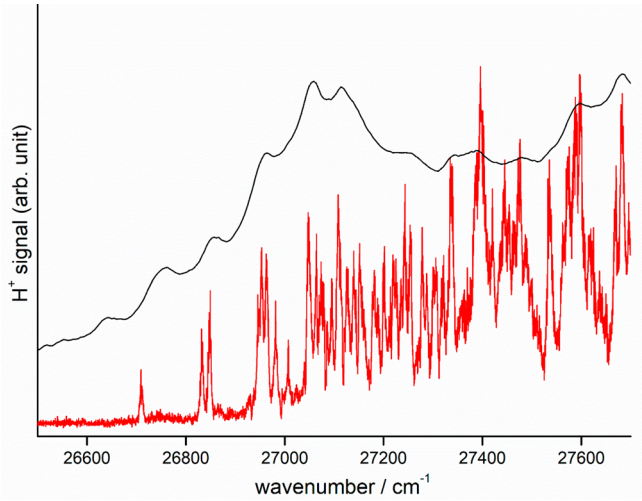

Figure 1. Molecular beam H-PFY spectrum of PA in He carrier gas (red) and room temperature absorption spectrum (black) adapted from data in ref 8.

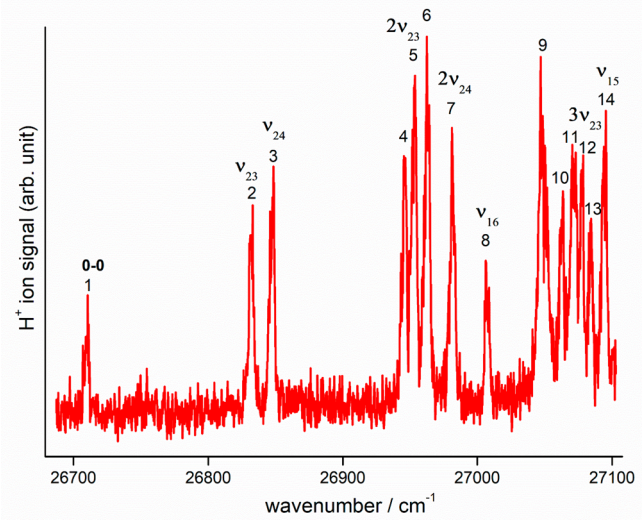

Figure 2. Molecular beam H-PFY spectrum of PA recorded in Ar carrier gas. Tentative assignments are marked.

mainly in the ground vibrational state of S_0. Also, the peak intensities depend on the dissociation efficiency from each vibrational level of S_1 to the monitored photofragment. In other words, the relative intensities of the peaks in the PFY spectra will not mimic the absorption spectrum if the photodissociation cross-section leading to the monitored product changes with excitation energy.

In order to assign the H-PFY spectrum, the contributions of the different conformers of PA must be assessed. The two relevant conformers of ground state PA are shown in Figure 3. The most stable conformer, Tc, which comprises 87% of the population at room temperature, lies 730 cm^{-1} below the Tt conformer (the barrier height for Tc to Tt isomerization is unknown).[18] Although gas-phase IR studies show the presence of both Tc and Tt conformers at room temperature, the contribution of the Tt conformer to the recorded spectrum is reported to be significantly lower than the Tc conformer, reflecting the large population difference of the two conformers.[19]

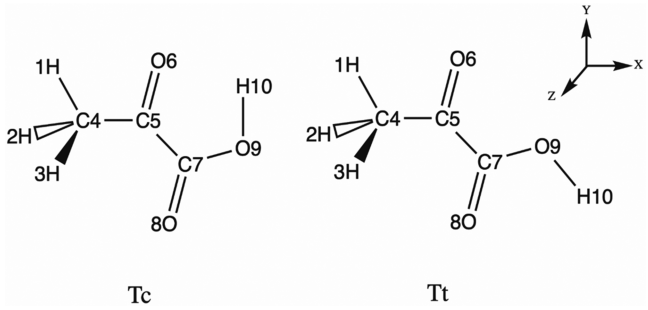

Figure 3. Tc and Tt conformers of PA identified in previous studies.[18,19] The Tc conformer is more stable than the Tt due to intramolecular H bonding.

In order to investigate the contribution of the Tt conformer in our molecular beam experiments, the H-PFY spectrum was recorded with different heating conditions of the PA sample prior to expansion. The H-PFY spectra recorded when PA was heated to 298, 318, and 338 K did not exhibit new peaks or differences in peak intensities. On the basis of the large difference in population between the Tc and the Tt conformers of S_0 and the apparent temperature independence of the H-PFY spectrum, we conclude that the H-PFY spectrum recorded in our study represents primarily absorption by the Tc conformer of PA.

To confirm that the H-PFY spectrum is a fingerprint of the molecular beam $S_1 \leftarrow S_0$ absorption spectrum of PA, CH_3CO (mass 43) and HOCO (mass 45) products were detected in one-color multiphoton experiments (section II), and as seen in Figure S1 in the Supporting Information, their PFY spectra match well the H-PFY spectrum.

III.B. Reaction Thermochemistry and Fragments' Kinetic Energy Release. In order to obtain a comprehensive view of the photodissociation dynamics of PA, time-sliced images of the fragments were recorded at excitation energies corresponding to several peaks in the H-PFY spectrum. As seen below, the high KER of fragments observed following excitation to the ground vibrational level of S_1 (26 710 cm^{-1}) indicates that the detected products are generated by two-photon dissociation. Therefore, we need to estimate the thermochemical heats of reaction (ΔH_{rxn}) of the reactions that may give rise to the observed products. As discussed in section IV, both two- and three-body fragmentation processes are energetically allowed. ΔH_{rxn} values for the relevant reactions, which are accurate to within 400 cm^{-1}, are listed in cm^{-1} below.

$$CH_3COCOOH \rightarrow CH_3CO + HOCO \quad \Delta H_{rxn} = 28\,600 \tag{1}$$

$$CH_3COCOOH \rightarrow CH_3CO + H + CO_2 \quad \Delta H_{rxn} = 28\,900 \tag{1a}$$

$$CH_3COCOOH \rightarrow CH_3CO + OH + CO \quad \Delta H_{rxn} = 37\,600 \tag{1b}$$

$$CH_3COCOOH \rightarrow CH_3 + CO + HOCO \quad \Delta H_{rxn} = 31\,600 \tag{1c}$$

DOI: 10.1021/acs.jpca.9b04166
J. Phys. Chem. A 2019, 123, 5906−5917

$$CH_3COCOOH \rightarrow CH_2CO + H + HOCO$$
$$\Delta H_{rxn} = 42\,600 \quad (1d)$$

$$CH_3COCOOH \rightarrow CH_3COCOO + H \quad \Delta H_{rxn} = 39\,000 \quad (2)$$

$$CH_3COCOOH \rightarrow CH_2COCOOH + H$$
$$\Delta H_{rxn} = 33\,000 \quad (3)$$

$$CH_3COCOOH \rightarrow CH_3COCO + OH \quad \Delta H_{rxn} = 36\,700 \quad (4)$$

ΔH_{rxn} for reaction 1 has been calculated by Gabriel da Silva (private communication) and for reactions 2 and 3 by David Osborn (private communication). ΔH_{rxn} for reactions 1a−1c are estimated, respectively, by adding the reported ΔH_{rxn} values of HOCO → H + CO_2, HOCO → OH + CO, and CH_3CO → CH_3 + CO reactions to ΔH_{rxn} of reaction 1.[20,21] Alternatively, ΔH_{rxn} for these reactions can be estimated with similar results (within 400 cm^{-1} or better) from the heats of formation (ΔH_f^0) of reactants and products (see Table S1 in the Supporting Information). ΔH_{rxn} for reaction 1d is estimated from Table S1. ΔH_{rxn} for reaction 4 is estimated from ref 22.

The KER distributions of CH_3CO and H fragments and their corresponding recoil anisotropy parameters, β, are shown in Figures 4 and 5. We do not give center-of-mass (c.m.) KER values, because each product can be formed via more than one pathway.

The KER distributions of CH_3CO (Figure 4) exhibit two major components: a slow component peaking at around 200 cm^{-1}, and a fast component with a maximum around 2500 cm^{-1}. In addition, there is a tail that extends up to about 6500 cm^{-1}. The relative contribution of the high KER component increases with excitation energy, and the distribution becomes

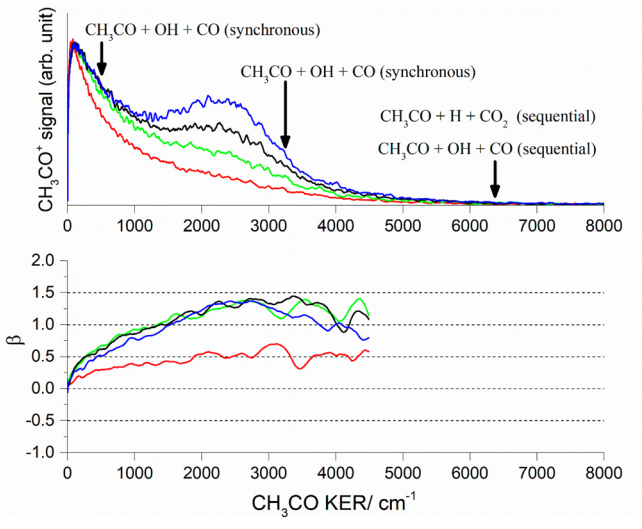

Figure 4. KER distributions (top) and corresponding recoil anisotropy parameters β (bottom) of the CH_3CO fragments following S_1 excitation in peaks 1, 3, 6, and 9 of the PFY spectrum in Figure 2 are shown in red, green, black, and blue, respectively. The KER distributions are normalized to the peak at low KER. The predicted KE_{max} values of CH_3CO produced via synchronous and sequential three-body fragmentation processes are marked by arrows. See the text for details.

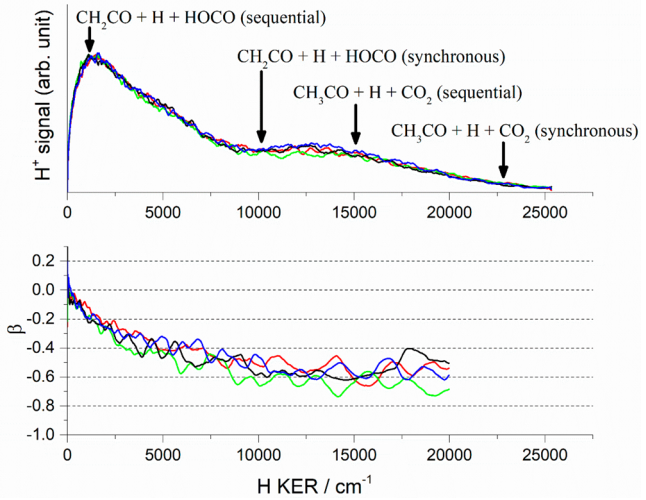

Figure 5. KER distributions (top) and corresponding recoil anisotropy parameters β (bottom) of H fragments following S_1 excitation in peaks 1, 3, 6, and 9 of the PFY spectrum in Figure 2 are shown in red, green, black, and blue, respectively. The predicted KE_{max} values for synchronous and sequential three-body fragmentation processes are marked by arrows. See the text for details.

clearly bimodal. The β parameter calculated for each of the distributions is shown as a function of KER in the lower panel of Figure 4. At low kinetic energies, the average value of β increases from 0.2 to 0.5 with increasing excitation energy. However, once the high KER component becomes dominant, its β value stays constant at 1.4−1.5 for all excitation energies.

Similar to CH_3CO, the H-photofragment KER distributions are broad and multimodal, as shown in Figure 5. They extend up to ∼25 000 cm^{-1} with three apparent features centered at about 1500, 5000, and 13 000 cm^{-1}. The angular distribution of the lowest KER component is nearly isotropic (β = 0 to −0.2) but it progressively becomes more anisotropic at higher kinetic energies (β = −0.4 to −0.6).

Other detected products were CO, HOCO, and CH_3. The KER distribution of ground state CO ($X\ ^1\Sigma^+$, v″ = 0, bandhead) was recorded following excitation of PA in peak 1 of Figure 2 and is shown in Figure 6. A small signal at mass 45 was observed in a one color experiment and assigned to HOCO. Its measured KER distribution is shown in Figure 7.

We were able to detect CH_3 radicals in one-color experiments. The 2+1 REMPI spectra of CH_3 indicate the formation of CH_3 products in the ground ($v_1''\ v_2''\ v_3''\ v_4''$ = 0000) and excited ($v_1''\ v_2''\ v_3''\ v_4''$ = 0100) vibrational levels. Images of CH_3 ($\tilde{X}\ ^2A_2''$, 0000) and CH_3 ($\tilde{X}\ ^2A_2''$, 0100) were recorded at 333.77 (0_0^0) and 329.95 (2_1^1) nm, respectively, and the corresponding KER distributions are shown in Figure S2 of the Supporting Information. Attempts to detect CH_3 in a two-color pump−probe experiment were unsuccessful because the large probe-only signal masks the pump−probe signal of the CH_3 product. This is because the absorption cross section of PA at the probe wavelength (325−336 nm) is much greater than that at the 369−374 nm pump wavelength.[8]

All the detected fragments exhibit high kinetic energies, much higher than allowed in one-photon absorption, while their PFY spectra have features characteristic of absorption to the S_1 state. We conclude, therefore, that the products are formed by two-photon absorption via the S_1 state. This interpretation is supported by the quadratic dependence of the

DOI: 10.1021/acs.jpca.9b04166
J. Phys. Chem. A 2019, 123, 5906−5917

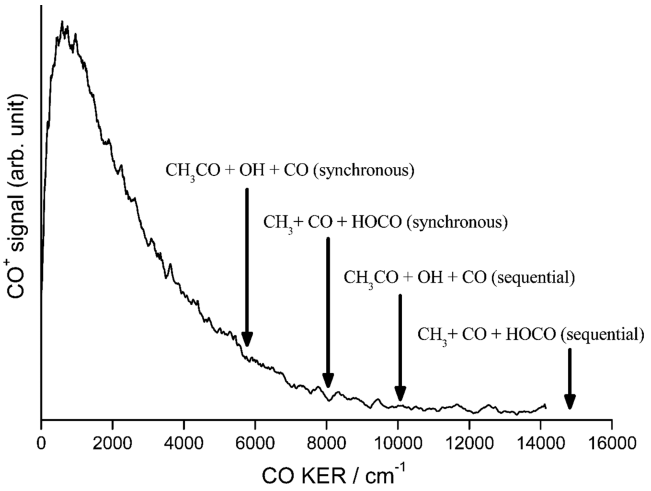

Figure 6. KER distribution of CO fragments ($X\ ^1\Sigma^+$, $v'' = 0$, bandhead) detected by 2+1 REMPI at 230.1 nm following the excitation of PA in peak 1 of Figure 2. The predicted KE_{max} values for synchronous and sequential three-body fragmentation processes are marked by arrows. See the text for details.

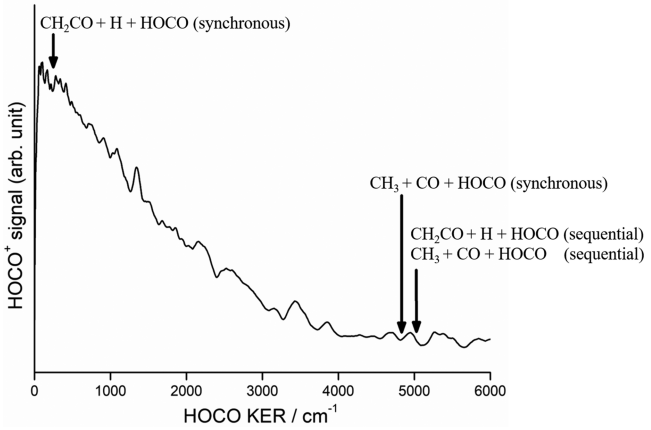

Figure 7. KER distribution of HOCO following S_1 excitation in peak 9 of Figure 2. The predicted KE_{max} values of HOCO produced by three-body synchronous and sequential fragmentation processes are marked by arrows. See the text for details.

H-photofragment signal on pump laser fluence. The excitation and dissociation mechanisms leading to the observed products are discussed in detail in the next section.

IV. DISCUSSION

IV.A. Electronic Structure Calculations of Excited States of PA. As discussed above, the observed products are generated by two-photon absorption followed by dissociation of PA. In order to characterize the excited electronic states accessed by two-photon absorption, the vertical excitation energies from S_0 to the S_1–S_3 states, the oscillator strengths of the relevant transitions, and the directions of their transition dipole moments have been calculated at the EOM-EE-CCSD/6-311(2+)G** level of theory, and are listed in Table 1. The vertical excitation energies from S_0 to S_1–S_3 are in good agreement with previous calculations.[22]

The two-photon excitation energy reached via the origin (0–0) band of S_1 is 53 420 cm^{-1} (see section III.B), which is higher than the calculated vertical $S_2 \leftarrow S_0$ excitation energy

Table 1. Calculated Vertical Excitation Energies for the Indicated Transitions, Transition Dipole Moment Directions, and Oscillator Strengths Calculated Using EOM-EE-CCSD/6-311(2+)G [a]**

initial state	final state	transition type	vertical excitation energy/ cm^{-1}	transition dipole direction	oscillator strength
S_0	S_1	$\pi^* \leftarrow n_+$	29 850	perpendicular (Z)	6.0×10^{-5}
S_0	S_2	$\pi^* \leftarrow n_-$	45 160	perpendicular (Z)	1.6×10^{-4}
S_0	S_3	$\pi^* \leftarrow \pi$	56 500	parallel (X, Y)	7.0×10^{-2}
S_1	S_2		11 600	parallel (X, Y)	4.3×10^{-2}
S_1	S_3		26 050	perpendicular (Z)	2.8×10^{-5}

[a]The X, Y, and Z axes are defined with respect to the molecular plane, as shown in Figure 3.

(45 160 cm^{-1}); thus, the S_2 state can be accessed by two-photon absorption via S_1 at all the excitation energies. The oscillator strength for the $S_2 \leftarrow S_1$ transition is much larger than that for $S_3 \leftarrow S_1$, making this the most likely excitation process. Although the calculated $S_3 \leftarrow S_0$ vertical excitation energy is higher than the lowest two-photon excitation energy employed in this study (53 420 cm^{-1}), Dhanya et al. observed the formation of OH products in the photodissociation of PA at 193 nm (51 813 cm^{-1}) and concluded that both the S_2 and S_3 states can be reached at this energy.[22] In addition, we note that the $S_2 \leftarrow S_1$ transition is parallel whereas the $S_3 \leftarrow S_1$ transition is perpendicular. In the case of fast dissociation and axial recoil, the former should give rise to a recoil anisotropy parameter $\beta_{max} = 2$, whereas for the latter $\beta_{max} = -1$ is expected. In section IV.C we examine in detail the observed KER distributions and the recoil anisotropy in the photofragment images.

IV.B. $S_1 \leftarrow S_0$ Spectroscopy. In order to identify the origin band of the $S_1 \leftarrow S_0$ transition, H-PFY spectra were recorded at different sample temperatures, carrier gases, and backing pressures. The lowest energy peak (marked as 1 in Figure 2) appears consistently at 26 710 cm^{-1} under all conditions. We therefore assign this peak as the origin (0–0) band of the $S_1 \leftarrow S_0$ transition of the Tc conformer. Pressure and temperature dependence studies do not reveal hot bands in the H-PFY spectrum. The other resolved transitions and their positions relative to the 0–0 band are listed in Table S2 in the Supporting Information. Because the vibrational frequencies in the S_1 state of PA are unknown, only tentative assignments of the peaks in the H-PFY spectrum can be made at this time (see Figure 2). They are based on vibrational frequencies in the S_0 state and the geometries of S_0 and S_1. The relevant normal modes of S_0 are listed in Table S3 in the Supporting Informaiton.

The frequencies of the C5–C7 (υ_{24}) and CH_3 (υ_{23}) torsional modes in S_0 are 90 and 134 cm^{-1}, respectively.[23] The electronic structure calculations of Chang et al. show that the $S_1 \leftarrow S_0$ transition can be classified as $\pi^* \leftarrow n_+$, with the electron density in the S_1 state residing mainly along the central C5–C7 bond.[11] In addition, the calculated geometries of the S_0 and S_1 minima reveal that the C5–C7 bond is shortened significantly in S_1 compared to S_0. Therefore, it is reasonable to expect that the frequency of the torsional motion along the C5–C7 bond will increase in the S_1 state. A similar situation has been seen in glyoxal and methylglyoxal where the

DOI: 10.1021/acs.jpca.9b04166
J. Phys. Chem. A 2019, 123, 5906–5917

fundamental frequency of the corresponding torsional mode in S_1 is nearly double that in S_0.[24] On the basis of these observations, we tentatively assign peak 3 at 137 cm^{-1} relative to the 0−0 band as the C5−C7 torsion, υ_{24}, and peak 7 at 269 cm^{-1} relative to the 0−0 band as its overtone. The peak at 122 cm^{-1} relative to the 0−0 band (peak 2) is tentatively assigned as the fundamental of the CH_3 torsional mode, υ_{23}.

Tentative assignments of additional peaks marked in Figure 2 are listed in Table S2 in the Supporting Information. It is evident from Figure 2 that the two low frequency torsional modes cannot account for all the observed peaks in the PFY spectrum up to 400 cm^{-1} above the 0−0 peak. The unassigned peaks may correspond to internal rotations of the methyl group, which cause additional splittings of the bands. The role of methyl internal rotors in molecular spectroscopy has been studied extensively both experimentally and theoretically.[24−27] It is shown that the nondegenerate internal rotational modes of the methyl group give rise to split peaks that complicate spectral assignments. For example, peaks 4 and 6 (at 26 944 and 26 960 cm^{-1}, respectively) might represent additional splittings of $2\upsilon_{23}$ (peak 5; 26 952 cm^{-1}) caused by internal rotation of CH_3. The same might be true for peaks 10, 11, 13, and 14, which are adjacent to $3\upsilon_{23}$ (peak 12 at 27 078 cm^{-1}) with almost equal spacings. Peak 14 at 27 094 cm^{-1}, however, can be assigned also as the transition terminating in the CCO bending fundamental of S_1 (υ_{15}). High-level electronic structure calculations that include anharmonic vibrational frequencies and internal rotation of the methyl group are required in order to offer definite assignments.

IV.C. Two-Photon Dissociation. The ΔH_{rxn} values listed in section III.B indicate that both two- and three-body fragmentation processes are energetically accessible following two-photon absorption. In order to distinguish between the contributions of these processes, we turn our attention to the KER plots shown in Figures 4−7, focusing on the observed maximum KER values, KE_{max}, for each fragment.

IV.C.1. Two-Body Fragmentation Pathways. The maximum kinetic energy value, KE_{max}, of each fragment in the two-body fragmentation reactions 1−4 will be observed when the fragments have no internal energy. In the case of reaction 1, the maximum allowed c.m. kinetic energy is 53 400 − 28 600 cm^{-1} = 24 800 cm^{-1} for excitation via the ground vibrational level of S_1. In accordance with momentum conservation, the CH_3CO fragment can have KE_{max} = 12 700 cm^{-1}. Recalling that CH_3CO is not monitored state selectively, if CH_3CO is generated with internal energy close to its dissociation barrier of ∼6000 cm^{-1}, then its kinetic energy will reach only about 9600 cm^{-1}. The observed KE_{max} of CH_3CO, however, is only 6500 ± 500 cm^{-1} (Figure 4), indicating that the HOCO cofragment possesses significant internal energy. In the complementary KER measurement of HOCO shown in Figure 7, we find that the observed KE_{max} is 5000 ± 500 cm^{-1} (recorded at peak 4), which is, again, much smaller than the 12 100 cm^{-1} value expected for cold CH_3CO cofragments. This confirms that most CH_3CO fragments are internally hot. HOCO and CH_3CO fragments with internal energies exceeding their dissociation barriers will further dissociate leading to three-body fragmentation and these processes are discussed in the next section.

Primary H photofragments generated by reactions 2 and 3 have expected KE_{max} values of 14 000 ± 400 and 20 000 ± 400 cm^{-1}, respectively. Therefore, whereas C−H and O−H bond fission reactions might contribute to the observed KER distribution of H fragments (Figure 5), they are not likely to explain the observed KE_{max} of 23 000 cm^{-1}.

We conclude that two-body fragmentation processes alone cannot explain the observed KE_{max} of CH_3CO, HOCO, and H products, and we turn our attention to the contribution of three-body fragmentation processes.

IV.C.2. Three-Body Fragmentation Pathways: Synchronous and Sequential. Three-body fragmentation processes have been discussed in the literature extensively, and here we follow the treatment of Maul and Gericke,[28,29] who distinguish among what they term synchronous, sequential, and asynchronous processes. Synchronous three-body fragmentation refers to the simultaneous breaking of two bonds to produce three fragments. Sequential dissociation involves the initial breaking of one bond that results in two primary products, one of which has enough internal excitation to further dissociate. The asynchronous dissociation process is less well-defined; it involves breaking of the two bonds on time scales that differ by less than a rotational period of the molecule. This process will only be mentioned briefly in our discussion. Because we follow closely the treatment of Maul and Gericke, we list the equations describing the kinetic energy released in these processes in the Appendix and display the plots generated by using these equations in the Supporting Information (Figures S3−S5). Our goal is to estimate KE_{max} for the different pathways and compare the values with the observed KER plot of each fragment.

IV.C.2.a. Synchronous Three-Body Fragmentation. Obviously, KE_{max} will be observed when the three fragments are born with no internal energy. Therefore, we discuss here the fragmentation of an ABC molecule, where fragments A, B, and C have only kinetic energy. For synchronous dissociation, the fragments' KER distributions depend on the central A−B−C angle at the critical molecular geometry at the moment of fragmentation. In the case of PA, this geometry is unknown, but the anisotropy of the angular distributions (Figures 4 and 5) suggests that the final dissociation on S_2 (or S_3) is fast and direct. We therefore assume that the critical angle α during dissociation is similar to the corresponding bond angle in the S_1 state. Energy and linear momentum conservation dictate that

$$\vec{p_A} + \vec{p_B} + \vec{p_C} = 0 \quad \text{(I)}$$

$$E_A^{kin} + E_B^{kin} + E_C^{kin} = h\nu - \Delta H_{rxn} - \sum_{A,B,C} E_{int} = \epsilon \quad \text{(II)}$$

where $h\nu$ refers to the two photon energy; ΔH_{rxn} is the heat of reaction of the ABC molecule fragmenting into A, B, and C and leading to KER of E_A^{kin}, E_B^{kin}, and E_C^{kin}, respectively; E_{int} is the internal energy of the fragments, assumed here to be zero; and ϵ is the total available kinetic energy. The above equations can be solved to obtain the fragments' kinetic energies as a function of the angle α projected on the central atom. The analytical expressions for E_A^{kin}, E_B^{kin}, and E_C^{kin} with respect to α are listed in the Appendix (eqs AI−AIII).

For reactions 1b and 1c, α is defined as the angle C4C5C7 and C5C7O9, respectively, whereas α for reaction 1a can be estimated from the two angles C5C7O9 and C7O9H10 (see Figure S3 in the Supporting Information). A previous theoretical study reported that the C4C5C7 and C5C7O9 angles in S_1 are 119° and 115°, respectively, and these define the values of α for reactions 1b and 1c.[11] The C7O9H10 angle is 107°, leading to α = 42° for reaction 1a (see Figure S3 in the

DOI: 10.1021/acs.jpca.9b04166
J. Phys. Chem. A 2019, 123, 5906−5917

Supporting Information). Similarly, α for reaction 1d is calculated to be 49° considering the H1C4C5 (109°) and C4C5C7 (120°) angles and breaking of the C4−H1 bond, which lies in the molecular plane (see Figure S3 in the Supporting Information). We note that reaction 1d can also proceed by breaking the out-of-plane C4−H2 and C4−H3 bonds, which will result in different α values. However, we predict that KE_{max} of the H1, H2, and H3 fragments would be similar, because these values change only slightly with α for reaction 1d (see Figure S3 in the Supporting Information). The KE_{max} value for each fragment is obtained in this model by using ΔH_{rxn} for the appropriate reaction producing the fragment. These values are marked by arrows in Figures 4−7, listed in Table 2, and also shown in vertical dotted lines in Figure S3.

Table 2. Estimated Angle α and Corresponding KE_{max} Values of Fragments Produced via Synchronous Three-Body Fragmentation, Reactions 1a−1d[a]

reaction	α, deg	fragments	KE_{max}/cm^{-1}
1a	42	CH_3CO	529 ± 1
		CO_2	1802 ± 50
		H	22753 ± 50
1b	115	CH_3CO	3138 ± 140
		CO	5565 ± 500
		OH	7937 ± 360
1c	119	HOCO	4965 ± 50
		CO	8221 ± 860
		CH_3	14894 ± 50
1d	49	HOCO	229 ± 1
		CH_2CO	812 ± 29
		H	10300 ± 30

[a]The error bars for KE_{max} represent the deviations for a change of ±5° in the corresponding α value.

The estimated KE_{max} value of the H fragment generated in reaction 1a is close to the observed one, as shown in Figure 5, and so is the corresponding value for HOCO (Figure 7) generated in reaction 1c. The KE_{max} values for H and HOCO corresponding to reaction 1d are indicated in Figures 5 and 7, respectively. The observed values for CO (Figure 6) and CH_3CO (Figure 4), however, are lower than the predicted KE_{max} and might signify that either the fragments possess significant internal energy or they are generated by sequential processes.

IV.C.2.b. Sequential Three-Body Fragmentation. As discussed above, the KER plots displayed in Figures 4 and 7 indicate that CH_3CO and HOCO fragments produced via reaction 1 have significant internal energies. The observed KE_{max} values (6500 and 5000 cm^{-1}, respectively) leave up to ~13 300 cm^{-1} to distribute in internal energy of these fragments. In addition, noting that most CH_3CO and HOCO fragments have fairly low kinetic energies, some of their cofragments must have internal energies exceeding their dissociation barriers. ΔH_{rxn} for CH_3CO and HOCO dissociation reactions are listed below in cm^{-1}, with barrier heights listed in parentheses, if known.[20,21]

$$CH_3CO \rightarrow CH_3 + CO \quad \Delta H_{rxn} = 3000\ (6000) \tag{5}$$

$$CH_3CO \rightarrow CH_2CO + H \quad \Delta H_{rxn} = 14\,500 \tag{6}$$

$$HOCO \rightarrow OH + CO \quad \Delta H_{rxn} = 9000\ (\text{barrierless}) \tag{7}$$

$$HOCO \rightarrow H + CO_2 \quad \Delta H_{rxn} = 300\ (12\,000) \tag{8}$$

Considering again a triatomic ABC molecular analogue and assuming that, to achieve KE_{max} for each fragment, the final A, B, and C fragments must have no internal energy, we now look at the process: ABC → AB + C → A + B + C. We also take into account that KE_{max} will be achieved for collinear velocity vectors of the dissociating fragments, such that

$$|v_A| = |v_A^{CM} + v_{AB}| \quad \text{and} \quad |v_B| = |v_B^{CM} + v_{AB}|$$

The explicit equations, again following Maul and Gericke,[28] are given in the Appendix (eqs AIV−AXIV).

The internal energy of AB (E_{AB}^{int}) can be estimated from the c.m. KER in the first step. Therefore, the predicted KE_{max} value of each final product is plotted as a function of the c.m. KER in the first step by using eqs AXII−AXIV in the Appendix (see Figures S4 and S5 in the Supporting Information). The maximum possible KER in the first step refers to a scenario where the nondissociating fragment has zero internal energy and the dissociating fragment has internal energy just above its dissociation barrier. As the dissociating fragment internal energy increases above this value, the kinetic energy in the first step decreases concomitantly.

Figures S4 and S5 in the Supporting Information show the dependencies of KE_{max} of the nondissociating fragment and the products of the second dissociation step on the c.m. kinetic energy (or the internal energy of the dissociating product) generated in the first step. In our case, we determined whether a particular three-body fragmentation reaction is acceptable by comparing the observed and computed values of KE_{max} for the fragments in the first and second steps. For example, the observed KE_{max} values of the CH_3CO fragment is ~6500 cm^{-1} (Figure 4). For this value, we list in Table 3 the correlated

Table 3. Computed KE_{max} Values of Fragments Produced in the Secondary Reactions 5−8, Correlated with the Observed KE_{max} of CH_3CO or HOCO Generated in Reaction 1

reaction	observed KE_{max} of nondissociating fragment/cm^{-1}	correlated KE_{max} of fragments from secondary dissociation step/cm^{-1}
5	5000 (HOCO)	15000 (CO)
		17000 (CH_3)
6	5000 (HOCO)	5860 (CH_2CO)
		1940 (H)
7	6500 (CH_3CO)	10000 (CO)
		9500 (OH)
8	6500 (CH_3CO)	9000 (CO_2)
		15000 (H)

KE_{max} values expected for the products of the secondary dissociation of the HOCO cofragment to CO + OH and CO_2 + H (reactions 7 and 8). The KE_{max} values of the products of the secondary dissociation of CH_3CO (reactions 5 and 6), which are correlated with the observed ~5000 cm^{-1} KE_{max} value of the HOCO fragment (Figure 7), are also listed in Table 3. The predicted KE_{max} values are indicated by arrows in the KER plots of the CH_3CO, HOCO, CO, and H photofragments (Figure 4−7). Clearly, the sequential mechanism is consistent with the observed KE_{max} values of CH_3CO, HOCO, and possibly also CO.

DOI: 10.1021/acs.jpca.9b04166
J. Phys. Chem. A 2019, 123, 5906−5917

With these KE_{max} values of the synchronous and sequential fragmentation reactions in hand, we can now discuss the likely dissociation pathways following two-photon absorption of PA.

IV.C.3. Mechanistic Interpretations. The multimodal appearance of the KER distributions of the H and CH_3CO fragments suggests that more than one dissociation pathway contributes to the observed products. As discussed above, the fwhm of the H-PFY rovibronic bands (~4 cm^{-1}) indicates (taking into account that each band includes an unresolved rotational envelope) that the lifetime of the S_1 state is significantly longer than a picosecond. This lifetime is also consistent with the observation of light emission on the red side of the PA absorption spectrum. Consequently, PA in the S_1 state may undergo rotational and vibrational motions before absorbing another photon, and these motions will affect the product recoil anisotropy. Even though the interpretation of product angular distributions in multiple-photon dissociation is not straightforward, it is likely that the observed anisotropy is indicative of fast dissociation on S_2/S_3.

As shown in Table 2, the direction of the transition dipole moment for the $S_2 \leftarrow S_1$ transition is parallel with respect to the molecular plane whereas it is perpendicular for $S_3 \leftarrow S_1$. The high KER component of the CH_3CO distribution has a positive angular anisotropy parameter, β = 1.4−1.5, which is consistent with fast dissociation from the S_2 state. The slow KER component with smaller anisotropy, β = 0.2−0.5, may derive from dissociation of vibrationally excited PA in the S_1 or T_1 states reached via nonradiative transitions from S_2. The vibrational motions of PA involved in the couplings to lower electronic state(s) prior to dissociation can lead to reduction of the angular anisotropy of products. Internal conversion and intersystem crossings prior to dissociation are common in photodissociation of radicals and large polyatomic molecules, which often exhibit fast and slow kinetic energy components that are anisotropic and isotropic, respectively.[30−32] This scenario is also consistent with the increase in the fraction of the fast and anisotropic CH_3CO component with increasing excitation energy; at higher excitation energies, direct dissociation on S_2 may compete effectively with couplings to the lower electronic states.

Analysis of the angular distributions of the H fragment, which shows an overall negative anisotropy (β = −0.2 to −0.6), is more complicated because several two- and three-body fragmentation processes can contribute to H formation. For example, the angular distributions of H fragments produced via two-body O−H bond fission (reaction 2) and synchronous three-body fragmentation (reaction 1a) will depend on the angle between the transition dipole moment vector and the dissociating bond. Similarly, the angular distribution of H fragments produced via reaction 3 will be determined by the orientation of the dissociating methyl C−H bond relative to the transition dipole moment vector. However, the dissociation of rovibrationally hot HOCO to H + CO_2 (reaction 7) is likely to lead to H products with an isotropic angular distribution and a broad range of kinetic energies. We also cannot rule out that dissociation via the S_3 state (a perpendicular transition) may contribute to the observed value of β.

Taking into account the available energies for the different reactions, the KE_{max} values of the fragments, and the observed KER and angular distributions, we conclude that three-body fragmentation processes, synchronous and sequential, are major contributors to the CH_3CO, HOCO, H, and CO products generated by two-photon dissociation. At the two-photon energy of ~54 000 cm^{-1}, all the listed three-body fragmentation pathways are energetically allowed. While we have restricted the above discussion of the predicted KE_{max} values to synchronous and sequential three-body fragmentation processes, we note that asynchronous three-body fragmentation might also contribute to the observed KER distributions, but this mechanism is more difficult to evaluate without theoretical calculations. Nevertheless, analyses of the observed KE_{max} values show that three-body fragmentation pathways, both synchronous and sequential, can explain the observed KER plots of all the products most consistently.

Photoinduced three-body fragmentation has been observed previously in the photodissociation of molecules such as alkanes, alkenes, carbonyls, alcohols, and carboxylic acids.[33−48] In fact, it is quite common in molecules of the general formula CH_3COR, where R includes H, alkyl, halogens, cyanide, hydroxyl, and alkoxy.[14,28,29,34−44] For example, photodissociation studies of acetone reveal a sequential three-body fragmentation pathway, where nascent CH_3CO fragments further dissociate to CH_3 and CO.[14,35,45,46] Similar pathways have been observed in organic aldehydes such as formaldehyde, acetaldehyde, and higher analogues,[37,38,47] as well as in acetic acid and dihydroxybenzoic acid.[34,42] Synchronous three-body fragmentation has also been invoked in photodissociation of glyoxal, which is structurally similar to PA.[39,40,48] In the case of PA, R = COOH and both CO and CH_3 fragments can be observed in a sequential mechanism when the internal energy of the CH_3CO cofragment is above the barrier. In addition, as seen in Figure 4, synchronous processes can contribute to the lower kinetic energy components of the CH_3CO KER distribution.

It should also be borne in mind that the predicted KE_{max} values refer to cases when all the final dissociation fragments have zero internal energy. It is more realistic that many of the CH_3CO and HOCO products of reaction 1 would have nonzero internal energies. When this internal energy is lower than their dissociation barriers, stable HOCO and CH_3CO fragments will be observed. In general, the observed KER decreases when the reaction products have internal energy; therefore, internally hot fragments are correlated with KER values lower than the predicted KE_{max}.

Although we conclude that the S_2 state plays a major role in the formation of the observed products, the S_3 state might also contribute to the photodissociation. However, this contribution should be much smaller given the small oscillator strength and the perpendicular direction of the transition dipole moment of the $S_3 \leftarrow S_1$ transition.

In closing, we address briefly the issue of dissociation following $S_1 \leftarrow S_0$ excitation.[1−4,6,7] In previous studies, CO_2 was identified as a final dissociation product following one-photon excitation. Chang et al.[11] discuss the mechanism of decarboxylation following S_1 excitation in their electronic structure calculations (carried out at the CASSCF and MS-CASPT2 levels), which include conical intersections between the S_1, T_1, and S_0 states. They find that from the minimum energy geometry on S_1, which preserves the internal hydrogen bonding, hydrogen transfer from the carboxylic OH to the carbonyl O takes place on S_1 with a small barrier of 7.2 kcal/mol, resulting in a molecular structure that they call S1-HT-MIN. This transient species accesses efficiently an S_1/S_0 conical intersection that leads to decarboxylation on S_0. However, they also find that some molecules on S_1 reach a

DOI: 10.1021/acs.jpca.9b04166
J. Phys. Chem. A 2019, 123, 5906−5917

conical intersection with T_1 prior to H-transfer. Thus, they envision two minima on S_1 separated by a small barrier. It is likely, therefore, that the second photon absorption observed in the present work takes place from the first minimum, before H-transfer. The fast optical pumping rate achieved with the high fluence of pulsed and focused laser radiation (see section II) combined with the large oscillator strength of the $S_2 \leftarrow S_1$ transition makes this process competitive with H-transfer on S_1 followed by decarboxylation.

Our attempts to detect CO_2 using 3+1 REMPI schemes were unsuccessful for several reasons. First, CO_2 may be formed in many internal states, and the REMPI detection schemes that we tried were not sensitive enough to detect it state-selectively.[49] Second, the lifetime of S_1 may be long such that only a few molecules dissociate during the observation time window. Taking into account a molecular beam velocity of ~1400 m/s and a spot size of the focused probe laser of about 0.1 mm, we estimate the residence time of the molecules in the interaction region to be on the order of 100 ns. While the lifetime of the S_1 state is unknown, we note that light emission was observed upon excitation of room temperature samples,[1] and the linewidths observed in this study indicate a lifetime longer than a picosecond. While all these factors may contribute, it is most likely that the insensitivity of our REMPI detection scheme is the main reason we are unable to detect CO_2. In ongoing flow tube photodissociation experiments of room temperature PA following $S_1 \leftarrow S_0$ excitation, we have indeed succeeded in detecting nascent CO_2 products and the isomers of methylhydroxycarbene by using tunable VUV ionization. These results will be reported separately.

V. SUMMARY AND CONCLUSIONS

The first study of the photodissociation of PA in molecular beams is described providing information on the $S_1 \leftarrow S_0$ electronic spectroscopy of the Tc conformer, and the photodissociation products generated by two-photon dissociation via the S_1 state. The main results and conclusions are summarized below.

H-photofragment yield spectra at 330−380 nm reveal narrow rovibronic bands, which are well separated up to 400 cm^{-1} above the 26 710 cm^{-1} band origin. Progressions in the C−C and CH_3 torsional modes are tentatively assigned. The spectrum is complicated by splittings, which are probably due to the methyl group, and theoretical calculations are needed to confirm the assignments. From the linewidths of the vibronic bands, we conclude that the S_1 state lives longer than a picosecond, a result that is supported by the previous observation of light emission following $S_1 \leftarrow S_0$ excitation.

Electronic structure calculations show that the oscillator strength of the $S_2 \leftarrow S_1$ transition is more than 2 orders of magnitude larger than that of the $S_1 \leftarrow S_0$ transition, while the $S_3 \leftarrow S_1$ oscillator strength is much smaller (Table 2). We conclude that two-photon transitions via S_1 (mainly to S_2) are facile and, in fact, are difficult to suppress in focused laser experiments. This explains the generation of H, HOCO, CH_3CO, CO, and CH_3 photodissociation products in our study.

H, CO, and CH_3 fragments were detected by state-selective 2+1 REMPI, and HOCO and CH_3CO, by nonresonant multiphoton ionization. KER distributions of these fragments were determined, confirming the two-photon nature of the dissociation. The angular distributions of the H and CH_3CO products are anisotropic but show a dependence on KER. The anisotropy indicates that dissociation on the S_2 surface is fast.

Analyses of the energetically allowed dissociation pathways show that both two- and three-body fragmentation processes are feasible. While we cannot determine branching ratios, we have gained insight into the dissociation mechanisms by estimating the maximum allowed kinetic energy release, KE_{max}, of the fragments for synchronous and sequential three-body fragmentation pathways. These are compared to the computed KE_{max} values for two-body fragmentation processes and the observed KER distributions of the fragments. The analyses show that several three-body fragmentation processes, both synchronous and sequential, contribute significantly to the observed products. Also, most of the CH_3CO and HOCO fragments are generated with significant internal energy and many of them further dissociate. These results are hardly surprising in view of the high excess energy available for all the dissociation pathways.

APPENDIX

Synchronous and Sequential Three-Body Fragmentation. Following the procedure given by Maul and Gericke,[28] three-body fragmentation processes have been simulated for both synchronous and sequential three-body fragmentation of an ABC triatomic molecule, as described below.

Synchronous Fragmentation. For synchronous fragmentation, the energy distributions in the fragments depend on the central angle A−B−C at the moment of fragmentation (see Figure A1). Using energy and linear momentum conservation

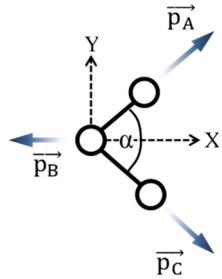

Figure A1. Schematic depiction of synchronous three-body fragmentation of a triatomic ABC molecule where two bonds break simultaneously. The *X*-axis is defined in the momentum vector space such that it lies along the central angle bisector of the planar molecule. The energy disposal in A, B, and C depends on the angle α at the critical configuration.

of the final products A, B, and C, as described in eqs I and II of the main text, the fragments' kinetic energies E_A^{kin}, E_B^{kin}, and E_C^{kin} are expressed as a function of α and the total available kinetic energy ϵ.

$$E_A^{kin} = \frac{\epsilon}{[(m_A + m_C)/m_C] + 4(m_A/m_B)\cos^2(\alpha/2)} \quad \text{(AI)}$$

$$E_B^{kin} = \frac{\epsilon}{[\{m_B(m_A + m_C)/4m_A m_C\}\sec^2(\alpha/2)] + 1} \quad \text{(AII)}$$

$$E_C^{kin} = \frac{\epsilon}{[(m_A + m_C)/m_A] + 4(m_C/m_B)\cos^2(\alpha/2)} \quad \text{(AIII)}$$

These equations are used to compute the KE_{max} values listed in Table 2 of the main text.

DOI: 10.1021/acs.jpca.9b04166
J. Phys. Chem. A 2019, 123, 5906−5917

Sequential Fragmentation. Unlike the synchronous three-body fragmentation case, where the calculated KE_{max} values of the products are determined solely by the angle α, the sequential case depends on the energy partitioning between the two steps and the fragment velocity vectors. The kinematics of a sequential three body fragmentation are shown in Figure A2.

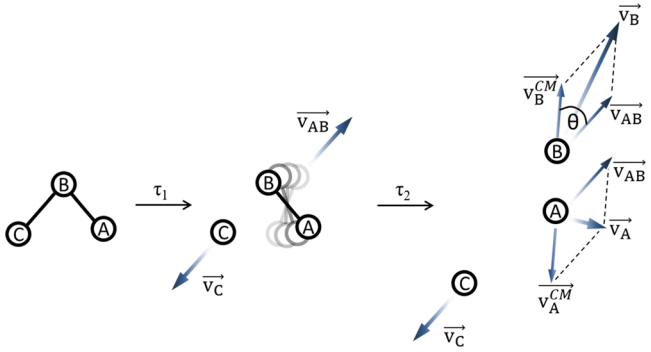

Figure A2. Schematic of sequential three-body fragmentation of ABC where the B−C bond breaks first at time τ_1 producing AB and C fragments. The AB fragment can further dissociate after time τ_2, which is longer than the mean rotational period of the AB intermediate. The observed laboratory-frame velocities of the A and B fragments depend on the velocity of AB.

Referring to Figure A2, the maximum kinetic energy release in the final products of a sequential process are derived by using,

$$h\nu - \Delta H_{rxn}^{step1} = E_C^{kin} + E_C^{int} + E_{AB}^{kin} + E_{AB}^{int} \quad \text{(AIV)}$$

$$E_{AB}^{int} - \Delta H_{rxn}^{step2} = E_A^{int} + E_A^{kin,CM} + E_B^{int} + E_B^{kin,CM} \quad \text{(AV)}$$

where ΔH_{rxn}^{step1} and ΔH_{rxn}^{step2} are the heats of reaction for the first and second fragmentation steps, respectively. When the maximum KER corresponds to zero internal energy in the fragments, the equations can be simplified to yield

$$h\nu - \Delta H_{rxn}^{step1} = E_C^{kin} + E_{AB}^{kin} + E_{AB}^{int} \quad \text{(AVI)}$$

$$E_{AB}^{int} - \Delta H_{rxn}^{step2} = E_A^{kin,CM} + E_B^{kin,CM} \quad \text{(AVII)}$$

During each fragmentation step, linear momentum is also conserved in the frame of reference of each step of bond breaking into two fragments. Therefore,

$$m_C\vec{v_C} + m_{AB}\vec{v_{AB}} = 0 \quad \text{(AVIII)}$$

$$m_A\vec{v_A^{CM}} + m_B\vec{v_B^{CM}} = 0 \quad \text{(AIX)}$$

Whereas eq AIX gives the velocities of A and B in the c.m. frame of AB, their laboratory frame velocities are obtained from the vector additions:

$$\vec{v_A} = \vec{v_A^{CM}} + \vec{v_{AB}} \quad \text{(AX)}$$

$$\vec{v_B} = \vec{v_B^{CM}} + \vec{v_{AB}} \quad \text{(AXI)}$$

In the limiting case where the fragments' velocity vectors in both dissociation steps are collinear ($\theta = 0$ in Figure A2), the maximum velocities of A and B are

$$|v_A| = |v_A^{CM} + v_{AB}| \quad \text{and} \quad |v_B| = |v_B^{CM} + v_{AB}|$$

Thus, the maximum fragment kinetic energies for a given first step AB with internal energy E_{AB}^{int} are

$$KE_{max}^{C} = \frac{(m_A + m_B)(h\nu - \Delta H_{rxn}^{step1} - E_{AB}^{int})}{(m_A + m_B + m_C)} \quad \text{(AXII)}$$

$$KE_{max}^{A} = \frac{1}{2}m_A\left(\sqrt{\frac{2m_C(h\nu - \Delta H_{rxn}^{step2} - E_{AB}^{int})}{(m_A + m_B + m_C)(m_A + m_B)}} + \sqrt{\frac{m_B(E_{AB}^{int} - \Delta H_{rxn}^{step1})}{m_A(m_A + m_B)}}\right)^2 \quad \text{(AXIII)}$$

$$KE_{max}^{B} = \frac{1}{2}m_B\left(\sqrt{\frac{2m_C(h\nu - \Delta H_{rxn}^{step2} - E_{AB}^{int})}{(m_A + m_B + m_C)(m_A + m_B)}} + \sqrt{\frac{m_A(E_{AB}^{int} - \Delta H_{rxn}^{step1})}{m_B(m_A + m_B)}}\right)^2 \quad \text{(AXIV)}$$

These equations are used to generate the values listed in Table 3, as explained in the main text.

■ ASSOCIATED CONTENT

Supporting Information

The Supporting Information is available free of charge on the ACS Publications website at DOI: 10.1021/acs.jpca.9b04166.

CH_3CO-PFY and HOCO-PFY spectra; KER plots of CH_3 fragments; heats of formation ($\Delta_f H^0$) of relevant species; tentative vibronic assignments for the $S_1 \leftarrow S_0$ transition; relevant vibrational frequencies of PA in S_0; simulated plots of KE_{max} for synchronous and sequential three-body fragmentation reactions of PA (PDF)

■ AUTHOR INFORMATION

Corresponding Author

*E-mail: reisler@usc.edu.

ORCID

Hanna Reisler: 0000-0003-0176-6131

Notes

The authors declare no competing financial interest.

■ ACKNOWLEDGMENTS

We thank Veronica Vaida (University of Colorado, Boulder) for illuminating discussions on the photodissociation pathways of pyruvic acid, and David Osborn (Sandia National Laboratories, Livermore) and Gabriel da Silva (The University of Melbourne, Melbourne) for helpful comments and providing results prior to publication. Support by the U.S. Department of Energy, Basic Energy Sciences, Grant No. DE-FG02-05ER15629 is gratefully acknowledged.

■ REFERENCES

(1) Yamamoto, S.; Back, R. The Photolysis and Thermal Decomposition of Pyruvic Acid in the Gas Phase. *Can. J. Chem.* **1985**, *63* (2), 549−554.

(2) Reed Harris, A. E.; Cazaunau, M.; Gratien, A.; Pangui, E.; Doussin, J. F.; Vaida, V. Atmospheric Simulation Chamber Studies of the Gas-Phase Photolysis of Pyruvic Acid. *J. Phys. Chem. A* **2017**, *121* (44), 8348−8358.

(3) Reed Harris, A. E.; Doussin, J. F.; Carpenter, B. K.; Vaida, V. Gas-Phase Photolysis of Pyruvic Acid: The Effect of Pressure on

DOI: 10.1021/acs.jpca.9b04166
J. Phys. Chem. A 2019, 123, 5906−5917

Reaction Rates and Products. *J. Phys. Chem. A* **2016**, *120* (51), 10123−10133.
(4) Reed Harris, A. E.; Pajunoja, A.; Cazaunau, M.; Gratien, A.; Pangui, E.; Monod, A.; Griffith, E. C.; Virtanen, A.; Doussin, J. F.; Vaida, V. Multiphase Photochemistry of Pyruvic Acid under Atmospheric Conditions. *J. Phys. Chem. A* **2017**, *121* (18), 3327−3339.
(5) Mellouki, A.; Mu, Y. On the Atmospheric Degradation of Pyruvic Acid in the Gas Phase. *J. Photochem. Photobiol., A* **2003**, *157* (2−3), 295−300.
(6) Vesley, G. F.; Leermakers, P. A. The Photochemistry of α-Keto Acids and α-Keto Esters. III. Photolysis of Pyruvic Acid in the Vapor Phase. *J. Phys. Chem.* **1964**, *68* (8), 2364−2366.
(7) Rosenfeld, R. N.; Weiner, B. Energy Disposal in the Photofragmentation of Pyruvic Acid in the Gas Phase. *J. Am. Chem. Soc.* **1983**, *105* (11), 3485−3488.
(8) Horowitz, A.; Meller, R.; Moortgat, G. K. The UV−VIS Absorption Cross Sections of the α-Dicarbonyl Compounds: Pyruvic Acid, Biacetyl and Glyoxal. *J. Photochem. Photobiol., A* **2001**, *146* (1−2), 19−27.
(9) Vaida, V.; Donaldson, D. J. Red-Light Initiated Atmospheric Reactions of Vibrationally Excited Molecules. *Phys. Chem. Chem. Phys.* **2014**, *16* (3), 827−836.
(10) Berges, M. G. M.; Warneck, P. Product Quantum Yields for the 350 nm Photodecomposition of Pyruvic Acid in Air. *Berichte Bunsenges. Für Phys. Chem.* **1992**, *96* (3), 413−416.
(11) Chang, X. P.; Fang, Q.; Cui, G. Mechanistic Photodecarboxylation of Pyruvic Acid: Excited-State Proton Transfer and Three-State Intersection. *J. Chem. Phys.* **2014**, *141* (15), 154311.
(12) Tjossem, P. J. H.; Smyth, K. C. Multiphoton Excitation Spectroscopy of the $B^1\Sigma^+$ and $C^1\Sigma^+$ Rydberg States of CO. *J. Chem. Phys.* **1989**, *91* (4), 2041−2048.
(13) Hudgens, J. W.; DiGiuseppe, T. G.; Lin, M. C. Two Photon Resonance Enhanced Multiphoton Ionization Spectroscopy and State Assignments of the Methyl Radical. *J. Chem. Phys.* **1983**, *79* (2), 571−582.
(14) Trentelman, K. A.; Kable, S. H.; Moss, D. B.; Houston, P. L. Photodissociation Dynamics of Acetone at 193 nm: Photofragment Internal and Translational Energy Distributions. *J. Chem. Phys.* **1989**, *91* (12), 7498−7513.
(15) Ryazanov, M.; Reisler, H. Improved Sliced Velocity Map Imaging Apparatus Optimized for H Photofragments. *J. Chem. Phys.* **2013**, *138* (14), 144201.
(16) Rodrigo, C. P.; Sutradhar, S.; Reisler, H. Imaging Studies of Excited and Dissociative States of Hydroxymethylene Produced in the Photodissociation of the Hydroxymethyl Radical. *J. Phys. Chem. A* **2014**, *118* (51), 11916−11925.
(17) Ryazanov, M.; Rodrigo, C.; Reisler, H. Overtone-Induced Dissociation and Isomerization Dynamics of the Hydroxymethyl Radical (CH_2OH and CD_2OH). II. Velocity Map Imaging Studies. *J. Chem. Phys.* **2012**, *136* (8), 084305.
(18) Reva, I. D.; Stepanian, S. G.; Adamowicz, L.; Fausto, R. Combined FTIR Matrix Isolation and Ab Initio Studies of Pyruvic Acid: Proof for Existence of the Second Conformer. *J. Phys. Chem. A* **2001**, *105* (19), 4773−4780.
(19) Plath, K. L.; Takahashi, K.; Skodje, R. T.; Vaida, V. Fundamental and Overtone Vibrational Spectra of Gas-Phase Pyruvic Acid. *J. Phys. Chem. A* **2009**, *113* (26), 7294−7303.
(20) Johnson, C. J.; Otto, R.; Continetti, R. E. Spectroscopy and Dynamics of the HOCO Radical: Insights into the OH + CO → H + CO_2 Reaction. *Phys. Chem. Chem. Phys.* **2014**, *16* (36), 19091−19105.
(21) Mordaunt, D. H.; Osborn, D. L.; Neumark, D. M. Nonstatistical Unimolecular Dissociation over a Barrier. *J. Chem. Phys.* **1998**, *108* (6), 2448−2457.
(22) Dhanya, S.; Maity, D. K.; Upadhyaya, H. P.; Kumar, A.; Naik, P. D.; Saini, R. D. Dynamics of OH Formation in Photodissociation of Pyruvic Acid at 193 nm. *J. Chem. Phys.* **2003**, *118* (22), 10093−10100.
(23) Hollenstein, H.; Akermann, F.; Günthard, Hs. H. Vibrational Analysis of Pyruvic Acid and D−, ^{13}C− and ^{18}O-Labelled Species: Matrix Spectra, Assignments, Valence Force Field and Normal Coordinate Analysis. *Spectrochim. Acta Part Mol. Spectrosc.* **1978**, *34* (11), 1041−1063.
(24) Kamei, S.; Okuyama, K.; Abe, H.; Mikami, N.; Ito, M. Mode Selectivity in Intersystem Crossing: Glyoxal, Methylglyoxal, and Biacetyl. *J. Phys. Chem.* **1986**, *90* (1), 93−100.
(25) Dawadi, M. B.; Perry, D. S. Communication: Conical Intersections between Vibrationally Adiabatic Surfaces in Methanol. *J. Chem. Phys.* **2014**, *140* (16), 161101.
(26) Wang, X.; Perry, D. S. An Internal Coordinate Model of Coupling between the Torsion and C−H Vibrations in Methanol. *J. Chem. Phys.* **1998**, *109* (24), 10795−10805.
(27) Gurnick, M.; Chaiken, J.; Benson, T.; McDonald, J. D. Vibrational and Rotational Spectroscopy of the First Electronically Allowed Transition of α-dicarbonyls. *J. Chem. Phys.* **1981**, *74* (1), 99−105.
(28) Maul, C.; Gericke, K. H. Photo Induced Three Body Decay. *Int. Rev. Phys. Chem.* **1997**, *16* (1), 1−79.
(29) Maul, C.; Gericke, K. H. Aspects of Photoinduced Molecular Three-Body Decay. *J. Phys. Chem. A* **2000**, *104* (12), 2531−2541.
(30) Amaral, G.; Xu, K.; Zhang, J. UV Photodissociation Dynamics of Ethyl Radical via the $\tilde{A}\,^2A'(3s)$ State. *J. Chem. Phys.* **2001**, *114* (12), 5164−5169.
(31) Song, Y.; Zheng, X.; Zhou, W.; Lucas, M.; Zhang, J. Ultraviolet Photodissociation Dynamics of the *n* -Propyl and *i* -Propyl Radicals. *J. Chem. Phys.* **2015**, *142* (22), 224306.
(32) Sun, G.; Song, Y.; Zhang, J. Ultraviolet Photodissociation Dynamics of 1-Pentyl Radical. *Chin. J. Chem. Phys.* **2018**, *31* (4), 439−445.
(33) Maul, C.; Haas, T.; Gericke, K. H. Photoinduced Near Ultraviolet Three Body Decay of Phosgene. *J. Phys. Chem. A* **1997**, *101* (36), 6619−6632.
(34) Hunnicutt, S. S.; Waits, L. D.; Guest, J. A. $^1(n, \pi^*)$-Photochemistry of Acetic Acid at 200 nm: Further Evidence for an Exit Channel Barrier and Reaction Selectivity. *J. Phys. Chem.* **1991**, *95* (2), 562−570.
(35) North, S. W.; Blank, D. A.; Gezelter, J. D.; Longfellow, C. A.; Lee, Y. T. Evidence for Stepwise Dissociation Dynamics in Acetone at 248 and 193 nm. *J. Chem. Phys.* **1995**, *102* (11), 4447−4460.
(36) Tsai, P.-Y.; Chao, M. H.; Kasai, T.; Lin, K.-C.; Lombardi, A.; Palazzetti, F.; Aquilanti, V. Roads Leading to Roam. Role of Triple Fragmentation and of Conical Intersections in Photochemical Reactions: Experiments and Theory on Methyl Formate. *Phys. Chem. Chem. Phys.* **2014**, *16* (7), 2854−2865.
(37) Hobday, N.; Quinn, M. S.; Nauta, K.; Andrews, D. U.; Jordan, M. J. T.; Kable, S. H. Experimental and Theoretical Investigation of Triple Fragmentation in the Photodissociation Dynamics of H_2CO. *J. Phys. Chem. A* **2013**, *117* (46), 12091−12103.
(38) Morajkar, P.; Bossolasco, A.; Schoemaecker, C.; Fittschen, C. Photolysis of CH_3CHO at 248 nm: Evidence of Triple Fragmentation from Primary Quantum Yield of CH_3 and HCO Radicals and H Atoms. *J. Chem. Phys.* **2014**, *140* (21), 214308.
(39) Osamura, Y.; Schaefer, H. F.; Dupuis, M.; Lester, W. A. A Unimolecular Reaction ABC→A+B+C Involving Three Product Molecules and a Single Transition State. Photodissociation of Glyoxal: HCOHCO→H_2 + CO + CO. *J. Chem. Phys.* **1981**, *75* (12), 5828−5836.
(40) Scuseria, G. E.; Schaefer, H. F. The Unimolecular Triple Dissociation of Glyoxal: Transition-State Structures Optimized by Configuration Interaction and Coupled Cluster Methods. *J. Am. Chem. Soc.* **1989**, *111* (20), 7761−7765.
(41) North, S. W.; Marr, A. J.; Furlan, A.; Hall, G. E. Nonintuitive Asymmetry in the Three-Body Photodissociation of CH_3COCN. *J. Phys. Chem. A* **1997**, *101* (49), 9224−9232.
(42) Bagchi, A.; Dyakov, Y. A.; Ni, C. K. Photodissociation and Photoionization of 2,5-Dihydroxybenzoic Acid at 193 and 355 nm. *J. Chem. Phys.* **2010**, *133* (24), 244309.

DOI: 10.1021/acs.jpca.9b04166
J. Phys. Chem. A 2019, 123, 5906−5917

(43) Deshmukh, S.; Hess, W. P. Photodissociation of Acetyl Chloride: Cl and CH_3 Quantum Yields and Energy Distributions. *J. Chem. Phys.* **1994**, *100* (9), 6429−6433.
(44) de Wit, G.; Heazlewood, B. R.; Quinn, M. S.; Maccarone, A. T.; Nauta, K.; Reid, S. A.; Jordan, M. J. T.; Kable, S. H. Product State and Speed Distributions in Photochemical Triple Fragmentations. *Faraday Discuss.* **2012**, *157*, 227.
(45) Kim, S. K.; Pedersen, S.; Zewail, A. H. Direct Femtosecond Observation of the Transient Intermediate in the α-cleavage Reaction of $(CH_3)_2CO$ to $2CH_3$ + CO: Resolving the Issue of Concertedness. *J. Chem. Phys.* **1995**, *103* (1), 477−480.
(46) Zhong, Q.; Poth, L.; Castleman, A. W. Ultrafast Dissociation Dynamics of Acetone: A Revisit to the S_1 State and 3s Rydberg State. *J. Chem. Phys.* **1999**, *110* (1), 192−196.
(47) Chin, C. H.; Lee, S. H. Comparison of Two-Body and Three-Body Decomposition of Ethanedial, Propanal, Propenal, *n* -Butane, 1-Butene, and 1,3-Butadiene. *J. Chem. Phys.* **2012**, *136* (2), 024308.
(48) Hepburn, J. W.; Buss, R. J.; Butler, L. J.; Lee, Y. T. Molecular Beam Study of the Photochemistry of S_1 Glyoxal. *J. Phys. Chem.* **1983**, *87* (19), 3638−3641.
(49) Wu, M.; Johnson, P. M. A Study of Some Rydberg States of CO_2 by (3 + 1) Multiphoton Ionization Spectroscopy. *J. Chem. Phys.* **1989**, *91* (12), 7399−7407.

DOI: 10.1021/acs.jpca.9b04166
J. Phys. Chem. A 2019, 123, 5906−5917